Unmanned Ground Vehicle State Estimation using an Unmanned Air Vehicle

Dr. Donald K. MacArthur*, Dr. Carl D. Crane**

***Abstract*—Unmanned Air Vehicles (UAVs) have several advantages and disadvantages compared with Unmanned Ground Vehicles (UGVs). Both systems have different mobility and perception abilities. UAV systems have extended perception, tracking, and mobility capabilities compared with UGVs. UGVs have more intimate mobility and manipulation capabilities. This paper presents the research that has been conducted in the collaboration of UAVs and UGVs. This research demonstrates the use of a passive UAV system for tracking and state estimation of a UGV. This paper presents the UAV sensors and avionics, the algorithms for combining the UGV kinematics equations, and the geo-positioning algorithms used on the UAV to form a robust UGV state estimation. Experimental results are presented.**

I. Introduction

THE Center for Intelligent Machines and Robotics at the University of Florida has been performing autonomous ground vehicle research for over 15 years. In that time, research has been conducted in the areas of sensor fusion, precision navigation, precision positioning systems, and obstacle avoidance. Researchers have used small unmanned helicopters for remote sensing purposes for various applications. Recently, experimentation with unmanned aerial vehicles has been in collaboration with the Tyndall Air Force Research Laboratory at Tyndall AFB, Florida.

Recently, unmanned aerial vehicles (UAVs) have been used more extensively for military and commercial operations. The improved perception abilities of UAVs compared with unmanned ground vehicles (UGVs) make them more attractive for surveying and reconnaissance applications. A combined UAV/UGV multiple vehicle system can provide aerial imagery, perception, and target tracking along with ground target manipulation and inspection capabilities. This research investigates collaborative UAV/UGV systems and also demonstrates the application of a UAV/UGV system for various task-based operations.

The Air Force Research Laboratory at Tyndall Air Force Base has worked toward improving EOD and range clearance operations by using unmanned ground vehicle systems. This research incorporates the abilities of UAV/UGV systems to support these operations. The research vision for the range clearance operations is to develop an autonomous multi-vehicle system that can perform surveying, ordnance detection/geo-positioning, and disposal operations with minimal user supervision and effort.

*: Innovative Automation Technologies, LLC, Gainesville, FL

**: Professor and Laboratory Director, Center for Intelligent Machines and Robotics, Mechanical and Aerospace Engineering, University of Florida

II. Materials and Methods

A. Experimental Setup

The payload design provides a robust testing platform for this research. In order to improve the designs, vibration isolation of the payload from the aircraft was required as well as a data storage method that could withstand the harsh environment onboard the aircraft. The system schematic for the payload is shown in Figure 1.

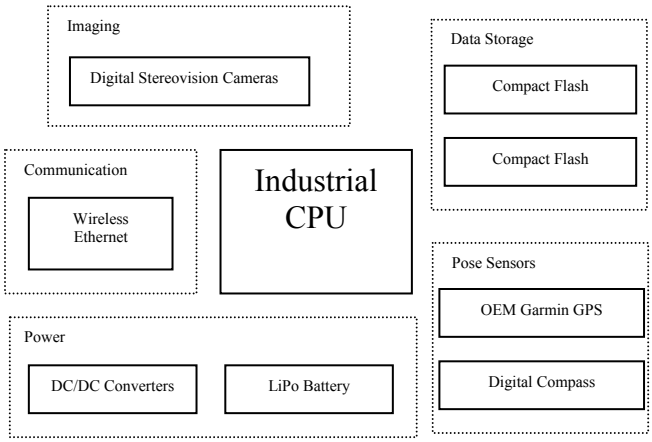

Fig. 1. Helicopter payload system schematic

The system consisted of six subsystems:

- Main processor
- Imaging
- Pose sensors
- Communication
- Data Storage
- Power

The payload contained an industrial CPU which utilized two compact flash drives for the operating system and data storage. The OEM Garmin GPS provided global position, velocity, and altitude data at 5Hz. The digital compass provided heading, roll, and pitch angles at 30Hz. The payload attached to aircraft landing gear is shown in Figure 2.

Fig. 2. Payload mounted to helicopter

Flight tests showed that the payload could reliably collect image and pose data during flight and maintain wireless communication at all times.

B. Camera Model

A precise camera model and an image to global coordinate transformation were developed. This involved finding the intrinsic and extrinsic camera parameters of the camera system attached to the aerial vehicle. A relation between the normalized pixel coordinates and coordinates in the projective coordinate plane was used:

$$\begin{Bmatrix} u_n \\ v_v \end{Bmatrix} = \begin{Bmatrix} \frac{X_c}{Z_c} \\ \frac{Y_c}{Z_c} \end{Bmatrix} \tag{1}$$

The normalized pixel coordinate vector $\tilde{m}$ and the projective plane coordinate vector $\tilde{M}$ are related using Equation 1 and from the projection relationship between points in the image plane and points in the camera reference frame as shown in Figure 3, where

$$\tilde{m} = \begin{Bmatrix} u_n \\ v_n \\ 1 \end{Bmatrix} \tag{2}$$

$$\tilde{M} = \begin{Bmatrix} X_c \\ Y_c \\ Z_c \\ 1 \end{Bmatrix}. \tag{3}$$

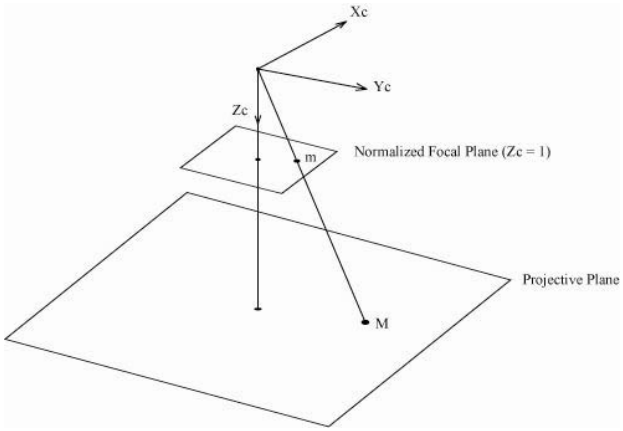

Fig. 3. Normalized focal and projective planes

The transformation from image coordinates to global coordinates was determined using the normalized pixel coordinates, and the camera position and orientation with respect to the global coordinate system (Figure 4). The transformation of a point M expressed in the camera reference system C to a point expressed in the global system is shown in Equation 4.

$$^{G}P_{M} = {}^{G}_{C}T \; {}^{C}P_{M} \tag{4}$$

$$^{G}P_{M} = \begin{Bmatrix} X_G \\ Y_G \\ Z_G \\ 1 \end{Bmatrix} = {}^{G}_{C}T \, {}^{C}P_{M} = \begin{bmatrix} {}^{G}_{C}R & {}^{G}P_{Co} \\ 0_3^T & 1 \end{bmatrix} \begin{Bmatrix} X_C \\ Y_C \\ Z_C \\ 1 \end{Bmatrix} \tag{5}$$

Dividing both sides of Equation 5 by Z_C and substituting $Z_G = 0$ (assuming the elevation of the camera is evaluated as the above ground level and the target location exists on the $Z_G = 0$ global plane) results in Equation 6.

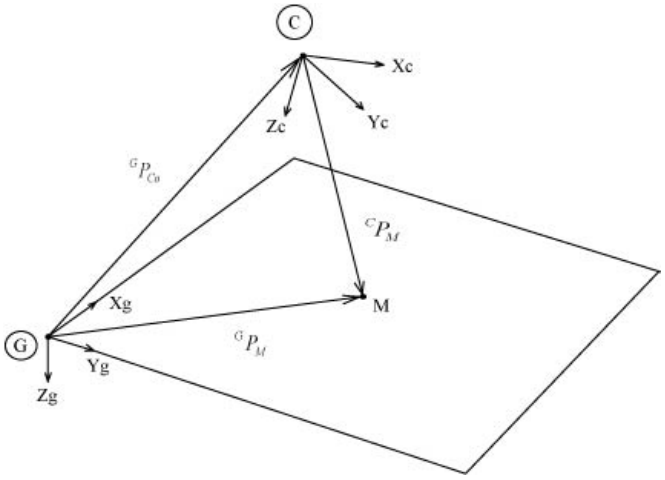

Fig. 4. Relation between a point in the camera and global reference frames

$$\begin{Bmatrix} \frac{X_G}{Z_C} \\ \frac{Y_G}{Z_C} \\ 0 \\ \frac{1}{Z_C} \end{Bmatrix} = \begin{bmatrix} {}^G_C R & {}^G P_{Co} \\ 0_3^T & 1 \end{bmatrix} \begin{Bmatrix} \frac{X_C}{Z_C} \\ \frac{Y_C}{Z_C} \\ 1 \\ \frac{1}{Z_C} \end{Bmatrix} \tag{6}$$

Substituting $X_C/Z_C = u_n$ and $Y_C/Z_C = v_n$:

$$\begin{Bmatrix} \frac{X_G}{Z_C} \\ \frac{Y_G}{Z_C} \\ 0 \\ \frac{1}{Z_C} \end{Bmatrix} = \begin{bmatrix} {}^G_C R & {}^G P_{Co} \\ 0_3^T & 1 \end{bmatrix} \begin{Bmatrix} u_n \\ v_n \\ 1 \\ \frac{1}{Z_C} \end{Bmatrix} \tag{7}$$

This leads to three equations and three unknowns X_G, Y_G, Z_C:

$$\frac{X_G}{Z_C} = R_{11}u_n + R_{12}v_n + R_{13} + \frac{{}^G P_{Cox}}{Z_C} \tag{8}$$

$$\frac{Y_G}{Z_C} = R_{21}u_n + R_{22}v_n + R_{23} + \frac{{}^G P_{Coy}}{Z_C} \tag{9}$$

$$0 = R_{31}u_n + R_{32}v_n + R_{33} + \frac{{}^G P_{Coz}}{Z_C} \tag{10}$$

where the scalar R_{ij} represents the element in the i[th] row and j[th] column of the R_{ij} matrix.

Using Equations 8, 9, and 10, Z_C, X_G, Y_G can be determined explicitly:

$$Z_C = \frac{-{}^G P_{Coz}}{R_{31}u_n + R_{32}v_n + R_{33}} \tag{11}$$

$$X_G = \left(\frac{-{}^G P_{Coz}}{R_{31}u_n + R_{32}v_n + R_{33}} \right) \left(R_{11}u_n + R_{12}v_n + R_{13} \right) + {}^G P_{Cox} \tag{12}$$

$$Y_G = \left(\frac{-{}^G P_{Coz}}{R_{31}u_n + R_{32}v_n + R_{33}} \right) \left(R_{21}u_n + R_{22}v_n + R_{23} \right) + {}^G P_{Coy} \tag{13}$$

Equations 12 and 13 provide the global coordinates of the static object.

C. Camera Calibration

In order to calculate the normalized pixel coordinates using raw imaging sensor data, a calibration procedure is performed using a camera calibration toolbox for MATLAB®[1]. The calibration procedure determines the extrinsic and intrinsic parameters of the camera system. During the calibration procedure, several images are used with checkerboard patterns of specific size that allow for the different parameters to be estimated.

The extrinsic parameters define the position and orientation characteristics of the camera system. These parameters are affected by the mounting and positioning of the camera relative to the body fixed coordinate system.

The intrinsic parameters define the optic projection and perspective characteristics of the camera system. These parameters are affected by the camera lens properties, imaging sensor properties, and lens/sensor placement properties. The camera lens properties are generally characterized by the focal length and prescribed imaging sensor size. The focal length is a measure of how strongly the lens focuses the light energy. This in essence correlates to the zoom of the lens given a fixed sensor size and distance. The imaging sensor properties are generally characterized by the physical size, and horizontal/vertical resolution of the imaging sensor. These properties help to define the dimensions and geometry of the image pixels. The lens/sensor placement properties are generally characterized by the misalignment of the lens and image sensor, and the lens to sensor planar distance. For our analysis we are mostly concerned with determining the intrinsic parameters of the camera system. These parameters are used for calculating the normalized pixel coordinates given the raw pixel coordinates.

The intrinsic parameters that are used for generating the normalized pixel coordinates are the focal length, principal point, skew coefficient, and image distortion coefficients. The focal length as described earlier estimates the linear projection of points observed is space to the focal plane. The focal length has components in the x and y axes and does not assume these values are equal. The principal point estimates the center pixel position. All normalized pixel coordinates are referenced to this point. The skew coefficient estimates the angle between the x and y axes of each pixel. In some instances the pixel geometry is not square or even rectangular. This coefficient describes how "off-square" the pixel x and y axes are and allows for compensation. The image distortion coefficients estimate the radial and tangential distortions typically caused by the camera lens. Radial distortion causes a changing magnification effect at varying radial distances. These effects are apparent when a straight line appears to be curved through the camera system. The tangential distortions are caused by ill centering or defects of the lens optics. These cause the displacement of points perpendicular to the radial imaging field.

The camera calibration toolbox allows for all of the intrinsic parameters to be estimated using several images of the predefined checkerboard pattern. Once the calibration procedure is completed, the intrinsic parameters are used in the geo-positioning algorithm. Selections of images were used that captured the checker pattern at different ranges and orientations.

The boundaries of the checker pattern were then selected manually for each image. The calibration algorithm used the gradient of the pattern to then find all of the vertices of the checkerboard.

Once the boundaries for all of the images were selected, the algorithm calculated the intrinsic camera parameter estimates using a gradient descent search. Using the selected images the following parameters were calculated:

Focal Length:

fc = [1019.52796 1022.12290] ± [20.11515 20.62667]

Principal point:

cc = [645.66333 527.72943] ± [13.60462 10.92129]

Skew:

alpha_c = [0.00000] ± [0.00000] => angle of pixel axes = 90.00000 ± 0.00000 degrees

Distortion:

kc = [-0.17892 0.13875 -0.00128 0.00560 0.00000] ± [0.01419 0.02983 0.00158 0.00203 0.00000]

Pixel error:

err = [0.22613 0.14137]

D. Coordinate Transformations

A body fixed coordinate system was used in order to relate sensor and motion information in the inertial and relative reference frames. Figures 5 and 6 show the body fixed coordinate system.

A transformation matrix was derived which relates the position and orientation of the body fixed frame to the inertial frame. The orientation of the body fixed frame is related to the inertial frame using a 3-1-2 rotation sequence. The inertial frame is initially in the North-East-Down orientation. The coordinates system undergoes a rotation ψ about the Z axis, then a rotation φ about the X' axis, and then a rotation θ about the Y'' axis. The compound rotation is equated below in Equation 14 and the subsequent rotations are shown in 15, 16, and 17.

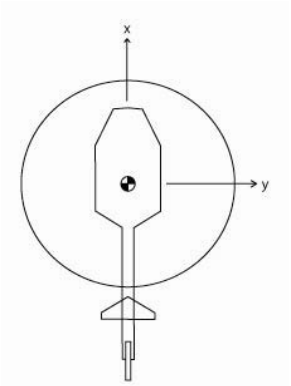

Fig. 5. Top view of the body fixed coordinate system

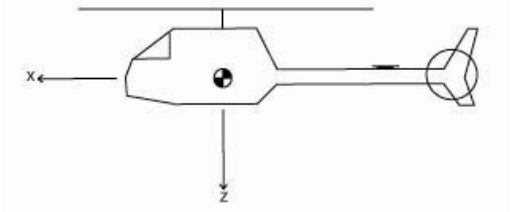

Fig. 6. Side view of the body fixed coordinate system

$$ {}^{1}R^{4} = {}^{1}R^{2}\,{}^{2}R^{3}\,{}^{3}R^{4} \tag{14} $$

$$ {}^{1}R^{2} = \begin{bmatrix} Cos\psi & Sin\psi & 0 \\ -Sin\psi & Cos\psi & 0 \\ 0 & 0 & 1 \end{bmatrix} \tag{15} $$

$$ {}^{2}R^{3} = \begin{bmatrix} 1 & 0 & 0 \\ 0 & Cos\phi & Sin\phi \\ 0 & -Sin\phi & Cos\phi \end{bmatrix} \tag{16} $$

$$ {}^{3}R^{4} = \begin{bmatrix} Cos\theta & 0 & Sin\theta \\ 0 & 1 & 0 \\ -Sin\theta & 0 & Cos\theta \end{bmatrix} \tag{17} $$

The final compound rotation matrix is equated below in Equation 18.

$$ {}^{1}R^{4} = \begin{bmatrix} C_\theta C_\psi + S_\theta S_\phi S_\psi & C_\theta S_\psi - S_\theta S_\phi C_\psi & S_\theta C_\phi \\ -C_\phi S_\psi & C_\phi C_\psi & S_\phi \\ -S_\theta C_\psi + C_\theta S_\phi S_\psi & -S_\theta S_\psi - C_\theta S_\phi C_\psi & C_\theta C_\phi \end{bmatrix} \tag{18} $$

where the notation C_i and S_i represent the Cosine and Sine of the angle *i* respectively.

The transformation matrix which converts a point measured in the body fixed frame to the point measured in the inertial fixed frame is shown in Equation 19.

$$ {}^{Inertial}T^{Body} = \begin{bmatrix} {}^{Inertial}_{Body}R & {}^{Inertial}P_{Bodyo} \\ 0_3^T & 1 \end{bmatrix} \tag{19} $$

where ${}^{Inertial}P_{Bodyo}$ represents the position of the body fixed frame origin measured in the inertial frame.

E. UGV State Estimation

The geo-positioning equations derived previously are restated below:

$$ \begin{Bmatrix} x_G \\ y_G \end{Bmatrix} = z_C A \tilde{b} \tag{20} $$

where

$$ \mathrm{A} = \begin{bmatrix} C_\theta C_\psi + S_\theta S_\phi S_\psi & C_\theta S_\psi - S_\theta S_\phi C_\psi & S_\theta C_\phi & {}^{G}P_{Co_x} \\ -C_\phi S_\psi & C_\phi C_\psi & S_\phi & {}^{G}P_{Co_y} \end{bmatrix} \tag{21} $$

$$ \tilde{b} = \begin{pmatrix} u_n \\ v_n \\ 1 \\ \dfrac{1}{z_c} \end{pmatrix} \tag{22} $$

$$ Z_C = \frac{-{}^{G}P_{Coz}}{R_{31}u_n + R_{32}v_n + R_{33}}. \tag{23} $$

By identifying two unique points fixed to the UGV, the direction vector can be defined:

$$\hat{h} = \begin{Bmatrix} Cos(\psi) \\ Sin(\psi) \end{Bmatrix}$$

$$\hat{h} = \begin{Bmatrix} \left(\dfrac{x_{G2} - x_{G1}}{\left(x_{G2} - x_{G1}\right)^2 + \left(y_{G2} - y_{G1}\right)^2} \right) \\ \left(\dfrac{y_{G2} - y_{G1}}{\left(x_{G2} - x_{G1}\right)^2 + \left(y_{G2} - y_{G1}\right)^2} \right) \end{Bmatrix}$$

$$\hat{h} = z_C A \begin{pmatrix} u_{n2} - u_{n1} \\ v_{n2} - v_{n1} \\ 1 \\ \dfrac{1}{z_c} \end{pmatrix} \tag{24}$$

The heading of the vehicle can be found using:

$$\psi = \text{atan2}(Sin(\psi), Cos(\psi)) \tag{25}$$

The kinematic motion of the vehicle can be described by the linear and angular velocity terms. In the 2D case, the UGV is constrained to move in the x-y plane with only a z component in the angular velocity vector. Hence the state vector is shown below:

$$\tilde{x} = \begin{Bmatrix} \dot{x} \\ \dot{y} \\ \dot{\psi} \end{Bmatrix} = \begin{Bmatrix} vCos(\psi) \\ vSin(\psi) \\ \dot{\psi} \end{Bmatrix} = \begin{bmatrix} Cos(\psi) & 0 \\ Sin(\psi) & 0 \\ 0 & 1 \end{bmatrix} \begin{Bmatrix} v \\ \omega \end{Bmatrix} \tag{26}$$

In [2] the researchers define the kinematic equations for an Ackermann style UGV. Using these equations the kinematic equations are restated using our notation:

$$\begin{Bmatrix} \dot{x} \\ \dot{y} \end{Bmatrix} = \begin{Bmatrix} vCos(\psi) + \dfrac{\dot{\psi} L}{2} Sin(\psi) \\ vSin(\psi) - \dfrac{\dot{\psi} L}{2} Cos(\psi) \end{Bmatrix} \tag{27}$$

$$\begin{Bmatrix} \dot{x} \\ \dot{y} \end{Bmatrix} = \begin{bmatrix} Cos(\psi) & \dfrac{L}{2} Sin(\psi) \\ Sin(\psi) & -\dfrac{L}{2} Cos(\psi) \end{bmatrix} \begin{Bmatrix} v \\ \omega \end{Bmatrix}$$

Equation 27 follows the structure outlined in [3] and is rewritten in the form:

$$\tilde{z} = \begin{bmatrix} Cos(\psi) & \dfrac{L}{2} Sin(\psi) \\ Sin(\psi) & -\dfrac{L}{2} Cos(\psi) \end{bmatrix} \tilde{x} + \tilde{v} \tag{28}$$

$$\tilde{z} = H\tilde{x} + \tilde{v}$$

where $\tilde{z}$ is the measurement vector, $\tilde{x}$ is the state vector, and $\tilde{v}$ is the additive measurement error. The measurement error can be isolated and the squared error can be written in the form:

$$\begin{aligned} \tilde{v} &= \tilde{z} - H\tilde{x} \\ \tilde{v}^T \tilde{v} &= \left(\tilde{z} - H\tilde{x}\right)^T \left(\tilde{z} - H\tilde{x}\right) \end{aligned} \tag{29}$$

The measurement estimate is written in the form:

$$\hat{z} = H\hat{x} \tag{30}$$

Hence the sum of the squares of the measurement variations $z - \hat{z}$ is represented by:

$$J = \left(\tilde{z} - H\hat{x}\right)^T \left(\tilde{z} - H\hat{x}\right) \tag{31}$$

The sum of the squares of the measurement variations is minimized with respect to the state estimate as shown:

$$\begin{aligned} \frac{\partial J}{\partial \hat{x}} &= \frac{\partial \left(\tilde{z} - H\hat{x}\right)^T \left(\tilde{z} - H\hat{x}\right)}{\partial \hat{x}} \\ 0 &= \left(-H\right)^T \left(\tilde{z} - H\hat{x}\right) + \left(\tilde{z} - H\hat{x}\right)^T \left(-H\right) \\ 0 &= -H^T \tilde{z} + H^T H\hat{x} - \tilde{z}^T H + \hat{x}^T H^T H \\ 0 &= -2H^T \tilde{z} + 2H^T H\hat{x} \\ \hat{x} &= \left(H^T H\right)^{-1} H^T \tilde{z} \end{aligned} \tag{32}$$

Therefore the state estimate can be expressed as:

$$\begin{aligned} \hat{x} &= \left(\begin{bmatrix} Cos(\psi) & Sin(\psi) \\ \dfrac{L}{2} Sin(\psi) & -\dfrac{L}{2} Cos(\psi) \end{bmatrix} \begin{bmatrix} Cos(\psi) & \dfrac{L}{2} Sin(\psi) \\ Sin(\psi) & -\dfrac{L}{2} Cos(\psi) \end{bmatrix} \right)^{-1} \\ &\quad \begin{bmatrix} Cos(\psi) & Sin(\psi) \\ \dfrac{L}{2} Sin(\psi) & -\dfrac{L}{2} Cos(\psi) \end{bmatrix} \tilde{z} \\ \hat{x} &= \begin{bmatrix} 1 & 0 \\ 0 & -\dfrac{L^2}{4} \end{bmatrix}^{-1} \begin{bmatrix} Cos(\psi) & Sin(\psi) \\ \dfrac{L}{2} Sin(\psi) & -\dfrac{L}{2} Cos(\psi) \end{bmatrix} \tilde{z} \\ \hat{x} &= \begin{bmatrix} 1 & 0 \\ 0 & -\dfrac{4}{L^2} \end{bmatrix} \begin{bmatrix} Cos(\psi) & Sin(\psi) \\ \dfrac{L}{2} Sin(\psi) & -\dfrac{L}{2} Cos(\psi) \end{bmatrix} \tilde{z} \\ \hat{x} &= \begin{bmatrix} Cos(\psi) & Sin(\psi) \\ \dfrac{2}{L} Sin(\psi) & -\dfrac{2}{L} Cos(\psi) \end{bmatrix} \tilde{z} \end{aligned} \tag{33}$$

Equation 6-16 can be rewritten in the form:

$$\begin{Bmatrix} \hat{v} \\ \hat{\omega} \end{Bmatrix} = \begin{bmatrix} Cos(\psi) & Sin(\psi) \\ \dfrac{2}{L} Sin(\psi) & -\dfrac{2}{L} Cos(\psi) \end{bmatrix} \begin{Bmatrix} \dot{x} \\ \dot{y} \end{Bmatrix} \tag{34}$$

III. Experimental Results

The experimental results obtained using the Gas Xcell Aircraft equipped with a downward facing camera and the experimental payload discussed earlier were compared with simulation results using the estimated error distributions used in a Monte Carlo analysis. The testing conditions used for the simulation analysis are shown in Equation 35. The results show that the geo-positioning errors from simulation closely match the geo-positioning results obtained using the experimental vehicle/payload setup. The geo-positioning results are shown in Figure 7.

$$\{p\} = \begin{Bmatrix} {}^{G}P_{Co_x} = 0.0(m) \\ {}^{G}P_{Co_y} = 0.0(m) \\ {}^{G}P_{Co_z} = 10(m) \\ \phi = 0.0° \\ \theta = 0.0° \\ \psi = 0.0° \\ u_n = 0.0 \\ v_n = 0.0 \end{Bmatrix} \quad (35)$$

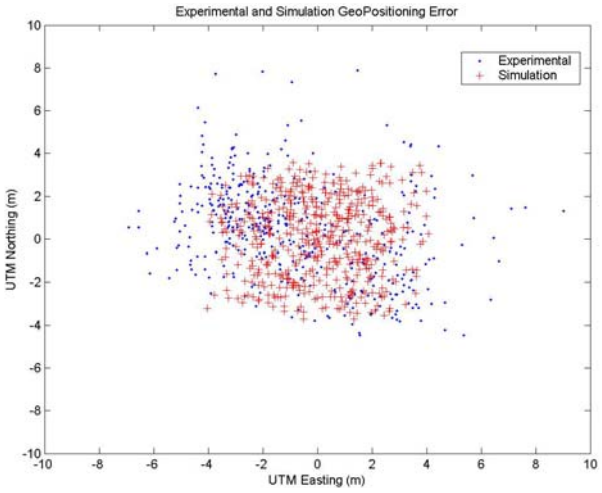

Figure 7. Experimental and simulation geo-position results

The use of a uniform error distribution for the simulation produces different results compared with a normal distribution. While the simulation results vary slightly from the experimental results, the uniform distribution provides more of an absolute bound for the error distribution.

IV. Future Work

This work will be applied to further UAV/UGV collaborative control experiments. Currently, a system is being developed that would allow for closed loop control of the UAV utilizing the state estimates of the UGV as feedback. The concept is to use the UGV state estimates to positioning the UAV above the UGV. This system would be useful for improving the UGV's perceptive and/or communication capabilities.

V. Conclusion

This paper has presented the research conducted for state estimation of an UGV using a passive UAV system. The UAV platform was discussed with details of system hardware and architecture. A simulated and experimental test was conducted to determine the geo-positioning accuracy using the aircraft system. Both data sets showed close distributions validating the simulation experiment. Also, the results show that the geo-positioning error is close to vendor specified positioning accuracy of the aircraft.

Acknowledgment

This research was conducted in collaboration with the Tyndall Air Force Base Robotics Research Laboratory in Panama City, Florida.

References

[1] Bouguet, J., Camera Calibration Toolbox for MATLAB®, http://www.vision.caltech.edu/bouguetj/calib_doc/

[2] .MacArthur, E., Crane, C., "Development of a Multi-Vehicle Simulator and Control Software", 2005 Florida Conference on Recent Advances in Robotics, Gainesville, Fl, 2005.

[3] The Analytic Sciences Corporation, "Applied Optimal Estimation", The MIT Press, Cambridge, Massachusetts, and London, England, 1974.

[4] Crane, C., Duffy, J., *Kinematic Analysis of Robot Manipulators*, Cambridge University Press, 1998.

[5] Faugeras, O., Luong, Q., *The Geometry of Multiple Images*, The MIT Press, 2001.